Pergamon

Int. Comm. Heat Mass Transfer, Vol. 23, No. 3, pp. 305–314, 1996

0735-1933/96 $12.00 + .00

PII S0735-1933(96)00016-4

MEASUREMENT OF TIME VARYING TEMPERATURE FIELDS USING VISIBLE IMAGING CCD CAMERAS

R. G. Keanini and C. A. Allgood
Department of Mechanical Engineering and Engineering Science
University of North Carolina at Charlotte
Charlotte, NC 28223, U.S.A.

(Communicated by J.P. Hartnett and W.J. Minkowycz)

ABSTRACT

A method for measuring time-varying surface temperature distributions using high frame rate visible imaging CCD cameras is described. The technique is based on an *ad hoc* model relating measured radiance to local surface temperature. This approach is based on the fairly non-restrictive assumptions that atmospheric scattering and absorption, and secondary emission and reflection are negligible. In order to assess performance, both concurrent and non-concurrent calibration and measurement, performed under dynamic thermal conditions, are examined. It is found that measurement accuracy is comparable to the theoretical accuracy predicted for infrared-based systems. In addition, performance tests indicate that in our experimental system, real-time calibration can be achieved while real-time whole-field temperature measurements require relatively course spatial resolution. The principal advantages of the proposed method are its simplicity and low cost. In addition, since independent temperature measurements are used for calibration, emissivity remains unspecified, so that a potentially significant source of error is eliminated.

Introduction

Planck's law shows that at surface temperatures less than ~5000 K, radiant emissive power reaches a maximum in the infrared ($0.76\ \mu m \leq \lambda \leq 1mm$) [1]. For this reason, photodetectors used in thermal imaging cameras typically incorporate semiconductor materials (e.g., PbSe and InSb) sensitive to IR radiation. Visible imaging systems, by contrast, employ semiconductor materials (e.g., Si and Ge) sensitive to visible radiation ($0.39 \leq \lambda \leq 0.76\ \mu m$). Since the latter class of photodetectors can exhibit significant response within a limited portion of the near infrared ($0.76 \leq \lambda \leq \sim 1.2\ \mu m$) [1,2], however, they can be used for surface temperature measurements [3].

Infrared-based methods (incorporating IR-sensitive photodetectors) for measuring surface temperature fields are described in a large literature (cf. [4-6]). In contrast, relatively few visible-based techniques

have been developed. Krause [7] describes an accurate visible radiometric method for measuring two-dimensional weld pool surface temperature distributions. Since this technique requires manual film processing and densitometry, however, real-time measurements are precluded [7]. Tenchov et al. [3] recently reported visible CCD-based measurements of steady-state temperature fields during electron beam evaporation. Measurements and calibration were based on an essentially *ad hoc* linear relationship between camera response and surface temperature. This is a valid approach and was indirectly validated using an independent measurement of overall evaporation rate. However, no direct assessment of measurement accuracy was provided. Chyu and Bizzak [8] recently described a laser-induced fluorescence technique for measuring surface temperatures. Here, a pulsed laser source excites a phosphor coated surface and induced fluorescence at two discrete visible lines is detected by an image-intensified CCD. Earlier, Goss et al. [9] used a similar method to determine surface temperatures on burning rocket propellant.

The objective of the present study is to develop a relatively simple, low cost, visible-based, real-time method for measuring time varying surface temperature fields. Our approach incorporates fairly non-restrictive assumptions, similar to those underlying a number of other techniques [3-8]: atmospheric absorption and scattering, and emission and reflection from secondary (non-target) sources are assumed negligible. In order to realistically assess the technique's potential utility, calibration and measurement, performed concurrently and non-concurrently, are carried out under dynamic conditions. In addition, parametric studies are undertaken in order to determine the method's performance.

System Model

Radiation incident on a sensor is comprised of radiation emitted and reflected from the target surface, radiation emitted and reflected from other surfaces and sources, and radiation scattered into the sensor by the intervening atmosphere. Each of these components is attenuated to varying degrees by absorption within the atmosphere. In deriving models of camera response to incident radiation, conservation of energy is typically used to formulate a generalized relationship between incident radiation and the various radiation components. Resultant models generally include empirical surface-, problem- and camera-specific functions that are either known, or require measurement or estimation [3,9,10].

In this work, scattering, atmospheric adsorption, and emission and reflection from secondary sources are assumed negligible. Under these conditions, the required model functions include the target's emissivity, the optical system's transmittance, and the camera's detectivity [2]. While detectivity and system transmittance are generally well characterized, target emissivity is typically unknown and variable. In order to bypass uncertainties associated with emissivity, we relate estimated local surface temperature, T_i, to local measured radiance, $\hat{L}_i$, using the following *ad hoc* model

$$T_i(\hat{L};\eta) = \sum_{n=1}^{N} \eta_n [\hat{L}_i]^{-n} \quad (1)$$

Here, i is an index referring to spatial location and η_n is the nth component of an N-dimensional parameter vector. The vector η is determined during calibration by minimizing the least square difference, Δ, between a set of calculated and independently measured temperatures [where Δ is defined in Eq. (6) below]. Depending on the application, the independent temperature measurements used for calibration can be obtained from one or more contact or non-contact temperature probes. In cases where emissivity exhibits spatial variation, independent measurements must be obtained at discrete points throughout the measurement domain. Notice that in addition to bypassing specification of emissivity, the model in Eq. (1) does not require specification of camera detectivity or optical system transmittance. As a potential means for improving accuracy, however, these latter quantities could be written as multiplicative functions on the right side of (1). Also note that in cases where atmospheric transmittance is not equal to 1, but is nevertheless uniform, the model implicitly accounts for atmospheric absorption. In cases where scattering, absorption and/or secondary emission and reflection are significant, a detailed model that explicitly accounts for each significant component must be formulated [10,11]. To allow real-time calibration, the model in Eq. (1) is specified as linear in η.

Experimental Procedures

The experimental setup is shown in Fig. 1. A propane torch is used to heat a square 100mm X 100mm X 3mm thick steel plate. The plate's front face is imaged using a high frame rate CCD camera (Dalsa CA-D1-0128) having specified optimal response over $0.4 \leq \lambda \leq 1.1 \mu m$. The camera signal is acquired and processed using a pc-based frame grabber (EPIX 4MEG Video Model 10) and supporting software (EPIX 4MIPD3.0-S). A typical image of the radiance distribution over the plate is shown in Fig. 2.

Eleven 1 mm diameter holes are drilled (perpendicularly) to a depth of 2.7 mm through the plate's back, non-imaged face. Type-K thermocouples (AWG 30) are then placed in each hole and held in place with thermally conductive paste (Omega Omegabond 200). To realistically assess whole field measurement error, and to allow for potential spatial variations in emissivity, the thermocouple array is spatially extended. The chosen arrangement allows capture of the entire range of surface temperatures at any given instant. Due to the plate's thinness, and due to the proximity of the thermocouples to the surface, we assume that the temperature measured by any given thermocouple is equal to the local front-face surface temperature. [Based on the temporal change in plate temperature during heating, it is estimated that the torch heat flux, q_o, is on the order of $10^5\ W\ m^{-2}$. Thus, the approximate difference, δT, in surface and sub-surface temperatures is on the order of $\delta T \sim q_o \delta / k \sim 1^{\circ}C$, where $\delta (= 0.3\ mm)$ is the

distance between a thermocouple bead and the front surface and k (= 30 $Wm^{-1}K^{-1}$ [12]) is the thermal conductivity.] The thermocouples are connected to a multiplexer (National Instruments AMUX 64T) which in turn is interfaced to a pc-based data acquisition board (National Instruments AT-MIO-16). Another type-K thermocouple (AWG 30), connected to a digital thermometer and placed in a twelfth hole (1.0 mm diameter, 2.7 mm depth), is used to monitor surface temperatures near the front face's center.

Since the data acquisition and frame grabber cards are housed on the same computer, calibration is performed in two successive runs. In both runs, the torch, which is kept at a fixed position and orientation, heats the plate from room temperature to a prespecified temperature T_o (= 710°C). Once T_o is achieved (where T_o is monitored using the digital thermometer), the torch is removed and thermocouple data (first run) and radiance data (second run) are obtained at M fixed time intervals, (Δt, $2\Delta t$,...,$M\Delta t$). Here, $\Delta t = t_e/M$, where t_e is the total elapsed time for any given experimental run. (In the following, an *experiment* consists of two successive *runs*, each performed under nominally identical conditions.) At each of the M sample points, thermocouple readings are obtained from all 11 thermocouples and stored on disk (where the thermocouple array is scanned at 100 kHz). Each of the corresponding M sets of radiance data consists of a single frame of the imaged plate, with each frame comprised of a 128X128 array of normalized pixel-level radiance values. The frame rate is fixed at 840 frames/s and surface oxides formed during heating are sanded off prior to each run. In addition, based on the frame grabber's 60 frame image buffer capacity, M=60 throughout.

In order to determine thermocouple locations in any given CCD image, five reference holes (2 mm diameter) are drilled through the plate. These appear as circular low radiance regions in Fig. 2. Normalized radiances from *single* pixels are used to define $\hat{L}_i$ in Eq. 1 since the 0.32 mm^2 plate area imaged by each pixel is comparable to the approximate 0.46 mm^2 cross-sectional area of each thermocouple bead. Averaging over groups of pixels may enhance calibration and measurement accuracy, but was not attempted here.

Calibration and Measurement

Three experiments were carried out over three different time intervals, $t_e^{(1)}$ = 0.071s, $t_e^{(2)}$ = 5s, and $t_e^{(3)}$ = 10s; for convenience we will refer to these experiments as experiment 1, 2 and 3. These times represent the range available for measurement, where the lower limit corresponds to the minimum time required to acquire and store 60(=M) frames, and the upper limit corresponds (approximately) to the maximum time that thermal radiation is detected by the camera.

To obtain acceptable (camera-based) temperature measurement accuracy, a range of intensities and

independent temperature measurements (obtained from thermocouples) must be included in the least square minimization procedure during calibration. Here, we use thermocouple temperatures and radiance data from the 10th, 20th and 30th samples in a given experiment (where, again, a total of M=60 samples are available in each of the three experiments). Thermocouple measurements and corresponding single-pixel radiances from these three samples are used to form the data vectors

$$\hat{\boldsymbol{T}}_s^{(\kappa)} = (\hat{T}_{s,1}^{(\kappa)},...,\hat{T}_{s,P}^{(\kappa)}), \quad \hat{\boldsymbol{L}}_s^{(\kappa)} = (\hat{L}_{s,1}^{(\kappa)},...,\hat{L}_{s,P}^{(\kappa)}) \quad \kappa = 1,2,3 \tag{2}$$

where superscript κ refers to the experiment number and P equals the number of thermocouples in the thermocouple array ($=N_T=11$) multiplied by the number of frames (=3) used in the minimization procedure (P = 33). Note that the data vectors represent subsets of the set of all thermocouple measurements, $\hat{\boldsymbol{T}}^{(\kappa)}$, and single-pixel radiance measurements, $\hat{\boldsymbol{L}}^{(\kappa)}$, obtained in each experiment, where

$$\hat{\boldsymbol{T}}^{(\kappa)} = (\hat{T}_1^{(\kappa)},...,\hat{T}_Q^{(\kappa)}), \quad \hat{\boldsymbol{L}}^{(\kappa)} = (\hat{L}_1^{(\kappa)},...,\hat{L}_Q^{(\kappa)}) \quad \kappa = 1,2,3 \tag{3}$$

and where Q ($= MxN_T$ =660) is the total number of measurements per experiment.

In considering different calibration and (camera-based) temperature measurement strategies, we find it convenient to define a slightly generalized form of Eq. (1):

$$T_i^{(\alpha\kappa)} = \sum_{n=1}^{N} \eta_n^{(\kappa)} [L_i^{(\alpha)}]^{-n} \quad \alpha,\kappa = 1,2,3 \tag{4}$$

Here, the set of camera-based temperature measurements has Q components, one for each of the Q measured single-pixel radiance values, $\hat{L}_i^{(\alpha)}$:

$$\boldsymbol{T}^{(\alpha\kappa)} = (T_1^{(\alpha\kappa)},...,T_Q^{(\alpha\kappa)}) \quad \alpha,\kappa = 1,2,3 \tag{5}$$

Equation (4) states that the ith camera-based temperature measurement, $T_i^{(\alpha\kappa)}$, is determined by inserting $\hat{L}_i^{(\alpha)}$ (from experiment α) and $\boldsymbol{\eta}^{(\kappa)}$ (from experiment κ) into Eq. (1). The three parameter vectors, $\boldsymbol{\eta}^{(1)}$, $\boldsymbol{\eta}^{(2)}$, and $\boldsymbol{\eta}^{(3)}$, determined during calibration, are obtained by minimizing the least square difference Δ between the reduced set of thermocouple measurements ($\hat{\boldsymbol{T}}_s^{(\kappa)}$) defined in Eq. 2, and the corresponding set of camera-based temperature measurements ($\boldsymbol{T}_s^{(\kappa\kappa)}$) derived from Eq. (4):

$$\Delta(\eta^{\kappa}) = \sum_{j=1}^{P} [\hat{T}_{s,j}^{(\kappa)} - T_{s,j}^{(\kappa\kappa)}(\eta^{(\kappa)})]^2 \tag{6}$$

As dictated by Eq. (4), $T_{s,j}^{(\kappa\kappa)} = \sum_{n=1}^{N} \eta_n^{(\kappa)} (\hat{L}_{s,j}^{(\kappa)})^{-n}$, where $\hat{L}_{s,j}^{(\kappa)}$ is the jth component of $\hat{\boldsymbol{L}}_s^{(\kappa)}$ [see Eq. (2)]. In all cases, minimization is performed using singular value decomposition. Calibration based on data from

experiments 1, 2 and 3 (producing $\boldsymbol{\eta}^{(1)}$, $\boldsymbol{\eta}^{(2)}$, and $\boldsymbol{\eta}^{(3)}$), will be referred to as short-, medium-, and long-interval calibration, respectively. In order to assess camera-based measurement accuracy, we will use the following error measure:

$$E^{(\alpha\kappa)} = \frac{1}{Q}\sum_{i=1}^{Q} \frac{|\hat{T}_i^{(\alpha)} - T_i^{(\alpha\kappa)}|}{\hat{T}_i^{(\alpha)}} \tag{7}$$

Results and Discussion

In the remainder of the paper, *measurement* will refer exclusively to camera-based temperature measurement. We first examine measurement accuracy associated with concurrent calibration and measurement. Here, temperatures $\boldsymbol{T}^{(\kappa\kappa)}$ are determined by substituting $\boldsymbol{\eta}^{(\kappa)}$ and $\hat{\boldsymbol{L}}^{(\kappa)}$ into Eq. (4). The associated errors, $E^{(\kappa\kappa)}$, are then calculated by inserting the camera-based and thermocouple-based temperatures, $\boldsymbol{T}^{(\kappa\kappa)}$ and $\hat{\boldsymbol{T}}^{(\kappa)}$, into Eq. (7). Based on this approach, we find that measurement accuracy is comparable to the theoretical accuracy predicted for commercial IR-based systems [10]. In the first experiment, for example (corresponding to $t_e^{(1)} = 0.071$ *s*), $E^{(11)} = 2.66$ %. Similarly, in the second and third experiments, corresponding to $t_e^{(2)} = 5$ *s* and $t_e^{(3)} = 10$ *s*, $E^{(22)} = 3.32$ % and $E^{(33)} = 4.55$ %, respectively. Refer to Fig. 3.

Considering next non-concurrent calibration and measurement, the most important question concerns determination of the optimal calibration interval. Steady state calibration allows sample averaging and thus improved parameter estimation. It is thus anticipated that dynamic calibration based on high sample rates would, by simulating steady state calibration, improve measurement accuracy. We test this idea in experiments 1 through 3 by determining measurement errors associated with short-, medium- and long-interval calibration (corresponding to $\boldsymbol{\eta}^{(1)}$, $\boldsymbol{\eta}^{(2)}$, and $\boldsymbol{\eta}^{(3)}$, respectively). The results shown in Fig. 3 support this notion. In particular, eliminating from consideration $E^{(11)}$, $E^{(22)}$ and $E^{(33)}$ (the errors associated with concurrent calibration and measurement), we find that the errors corresponding to short-interval calibration ($E^{(21)}$ and $E^{(31)}$) are lower than the errors associated with medium-interval ($E^{(12)}$ and $E^{(32)}$) and long-interval ($E^{(13)}$ and $E^{(23)}$) calibration. Similarly, errors associated with long-interval calibration are greater than those associated with short- and medium-interval calibration. Thus, in actual measurements, dynamic calibration over short time intervals provides optimal accuracy.

A significant goal of this work is to develop real time measurement and calibration capabilities (where *real-time* conventionally refers to operations performed in less than 1/30 s). An obvious strategy for

minimizing calibration and measurement time is to find the minimum number of basis functions (N) in $\eta^{(\kappa)}$ that provide an acceptable level of accuracy. Thus, incrementing N from 2 to 11, and performing short-, medium- and long-interval concurrent and non-concurrent calibration and measurement (in experiments 1 through 3), we find that in each of the nine cases depicted in Fig. 3, average error ($E^{(\alpha\kappa)}$) remains fixed, at the values shown in Fig. 3, over $4 \leq N \leq 11$. In order to assess associated changes in performance, calibration time, τ_c, is determined as a function of the number of basis functions, N, while measurement time, τ_m, is determined as a function of N and spatial resolution (τ_c does not depend on resolution). Here, τ_c is defined as $\tau_c = \max(S_I^{-1}, N_T S_T^{-1}) + \tau_\Delta$, where S_I is the camera frame rate (840 frames/s), S_T is the thermocouple data acquisition rate (100 kHz), N_T is the number of thermocouples (=11), and τ_Δ is the time required to minimize Δ in Eq. (6). Similarly, τ_m is defined as $\tau_m = 1/S_I + \tau_f$, where τ_f is the time required to calculate N_s X N_s temperatures from an N_s X N_s array of normalized, single frame radiances. Spatial resolution in this case is varied by defining 64 X 64, 32 X 32, and 16 X 16 sub-arrays from each frame's 128 X 128 pixel array (where rows and columns within any given sub-array correspond to equally spaced rows and columns within the 128 X 128 array).

Performance variations, with τ_f and τ_Δ calculated on a Sun Sparc 2 workstation, are shown in Fig. 4. It is clear that in the present system and over the range $4 \leq N \leq 11$, real-time calibration is possible. In contrast, real-time measurement can only be achieved at relatively course resolution, i.e., when $N_s = 16$ and $N \leq 10$, or when $N_s = 32$ and N = 4. It should be noted that real-time measurement at high spatial resolution might be achieved by parsing N_c sub-arrays to N_c parallel processors; this question will be addressed in a future publication. As would be expected, each two-fold increase in resolution (for any given N) results in an approximate four-fold increase in measurement time (see Fig. 4).

In summary, we have described a straightforward method for measuring time-varying surface temperature distributions using a high frame rate visible imaging CCD camera. It is found that measurement accuracy is comparable to the predicted accuracy of IR-based systems. The principal advantages of the proposed approach are its simplicity and low cost. Since independent pointwise temperature measurements are used for calibration, surface emissivity remains unspecified, so that a potentially significant source of measurement error is eliminated. The model defined in this study is applicable only in cases where scattering, atmospheric absorption, and emission and reflection from external sources are negligible. When one or more of these assumptions are violated, detailed physical modeling must be used to account for all significant radiation components.

Acknowledgements

Financial support provided by Oak Ridge Associated Universities, The Alcoa Foundation and the UNC Charlotte College of Engineering is gratefully acknowledged.

Nomenclature

$E^{(\alpha\kappa)}$ average relative measurement error in experiment α based on calibration in experiment κ

$\hat{L}$ measured normalized radiance

M number of samples

N number of parameters in η

N_s number of rows and columns in a sub-array

N_T number of thermocouples in the thermocouple array

Q number of thermocouple and single-pixel radiance measurements obtained in each experiment

S rate, s^{-1}

$t_e^{(\alpha)}$ duration of experiment α, s

$T^{(\alpha\kappa)}$ camera-based temperatures determined in experiment α from corresponding radiance measurements, based on calibration in experiment κ, K

$\hat{T}^{(\alpha)}$ thermocouple-based temperatures obtained in experiment α, K

Δ least square error between independently measured and camera-based temperatures

$\eta^{(\alpha)}$ N-dimensional parameter vector determined during calibration in experiment α

λ wavelength, μm

τ_c calibration time, s

τ_f time required to calculate $N_s \, X \, N_s$ temperatures from an $N_s \, X \, N_s$ array of normalized single-pixel radiances, s

τ_m measurement time, s

τ_Δ time required to minimize least square error Δ, s

References

1. B. E. A. Saleh and M. C. Teich, Fundamentals of Photonics, p. 663. Wiley, New York (1991).

2. J. H. Moore, C. C. Davis and M. A. Coplan, Building Scientific Apparatus, p. 265. Addison-Wesley, London (1983).

3. C. Tenchov, D. S. Simeonova, V. A. Mitev and N. Donkov, Meas. Sci. Technol. 4, 1050 (1993).

4. J. Hartikainen, Rev. Sci. Instrum. 60, 670 (1989).

5. J. E. Pacheco, R. M. Houser, and A. Neumann, Concepts to Measure Flux and Temperature for External Central Receivers, Proc. 1994 ASME/JSME/JSES International Solar Energy Conference, 595 (1994).

6. D. Holmsten and R. Houis, Proc. SPIE, 1313, 322 (1990).

7. H. G. Krause, Optics Lett., 11, 773 (1986).

8. M. K. Chyu and D. J. Bizzak, Rev. Sci. Instrum., 65, 102 (1994).

9. L. P. Goss, A. A. Smith and M. E. Post, Rev. Sci. Instrum., 60, 3702 (1989).

10. K. Chrzanowski, Appl. Optics, 34, 2888 (1995).

11. J. R. Schott, Photogrammetric Engrg. Remote Sensing, 55, 1311 (1989).

12. S. Kou and Y. H. Wang, Welding J., 65, 63s (1986).

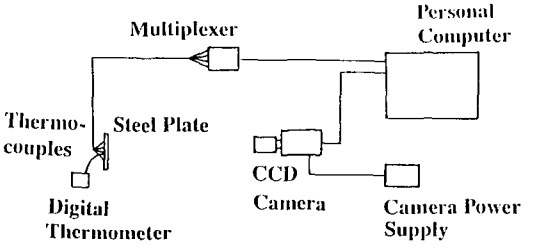

FIG. 1
Experimental system.

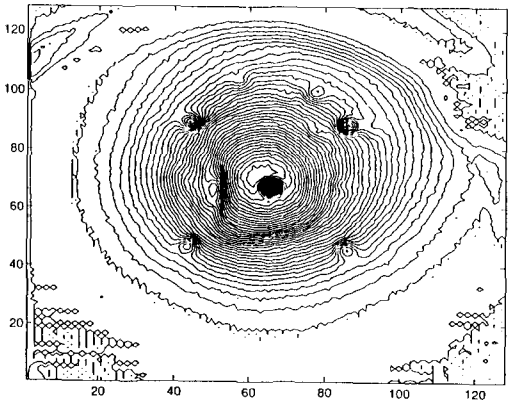

FIG. 2
Radiance distribution on plate. Pixel numbers are shown and imaged area is 72mm X 72mm.

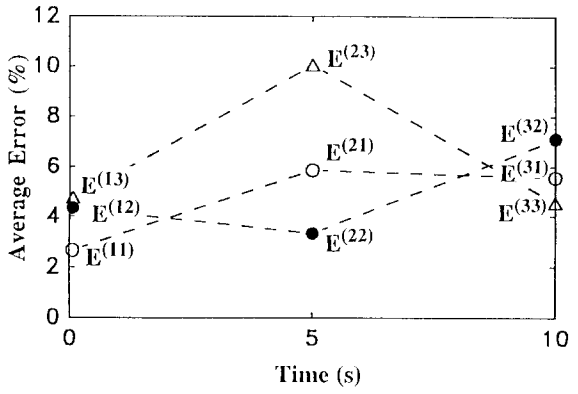

FIG. 3
Average measurement error. Repeating and non-repeating superscripts denote concurrent and non-concurrent calibration and measurement, respectively.

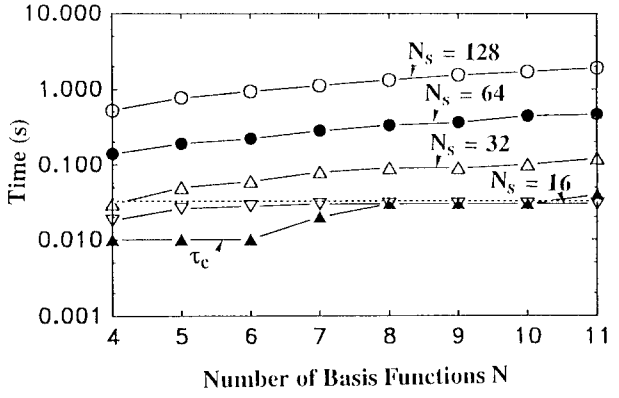

FIG. 4
Calibration and measurement time. Dashed line indicates real-time cut-off. Upper four plots (labeled by various N_s values) show measurement time at various levels of spatial resolution. Lowest plot shows calibration time.

Received October 6, 1995